The Astrophysical Journal, 743:124 (13pp), 2011 December 20 doi:10.1088/0004-637X/743/2/124

SUZAKU VIEW OF X-RAY SPECTRAL VARIABILITY OF THE RADIO GALAXY CENTAURUS A: PARTIAL COVERING ABSORBER, REFLECTOR, AND POSSIBLE JET COMPONENT

Yasushi Fukazawa, Kazuyoshi Hiragi, Syoko Yamazaki, Motohiro Mizuno, Kazuma Hayashi,
Katsuhiro Hayashi, Sho Nishino, Hiromitsu Takahashi, and Masanori Ohno
Department of Physical Science, Hiroshima University, 1-3-1 Kagamiyama, Higashi-Hiroshima, Hiroshima 739-8526, Japan;
fukazawa@hep01.hepl.hiroshima-u.ac.jp
Received 2011 July 12; accepted 2011 September 1; published 2011 November 29

ABSTRACT

We observed a nearby radio galaxy, Centaurus A (Cen A), three times with *Suzaku* in 2009 and measured the wide-band X-ray spectral variability more accurately than previous measurements. The Cen A was in an active phase in 2009, and the flux became higher by a factor of 1.5–2.0 and the spectrum became harder than that in 2005. The Fe–K line intensity increased by 20%–30% from 2005 to 2009. The correlation of the count rate between the XIS 3–8 keV and PIN 15–40 keV band showed a complex behavior with a deviation from a linear relation. The wide-band X-ray continuum in 2–200 keV can be fitted with an absorbed power-law model plus a reflection component, or a power law with a partial covering Compton-thick absorption. The difference spectra between high and low flux periods in each observation were reproduced by a power law with a partial covering Compton-thick absorption. Such a Compton-thick partial covering absorber was observed for the first time in Cen A. The power-law photon index of the difference spectra in 2009 is almost the same as that of the time-averaged spectra in 2005, but steeper by ∼0.2 than that of the time-averaged spectra in 2009. This suggests an additional hard power-law component with a photon index of <1.6 in 2009. This hard component could be a lower part of the inverse-Compton-scattered component from the jet, whose gamma-ray emission has recently been detected with the *Fermi* Large Area Telescope.

Key words: galaxies: active – galaxies: individual (Centaurus A) – galaxies: Seyfert – X-rays: galaxies

Online-only material: color figures

1. INTRODUCTION

Radio galaxies host extended emission from relativistic jets and lobes. Jet emission is extremely enhanced by relativistic effects for blazars, whose jet direction is close to the line of sight and observed in the multi-wavelength band from radio to TeV gamma rays. Recently, the *Fermi Gamma-ray Space Telescope* opened a new era for studying jet emissions by detecting more than 500 gamma-ray blazars (Abdo et al. 2010a). Furthermore, *Fermi* detected 10 radio galaxies and revealed that radio galaxies are also gamma-ray emitters (Abdo et al. 2010b). Radio galaxies are important for studying the jet structure from the misaligned jet direction; jet emissions of blazars are dominated by the central region of jets due to the beaming effect while those of radio galaxies are weighted by the jet outer boundary. Possible jet emission from radio galaxies has been reported from the infrared to the X-ray band (Chiaberge et al. 1999; Hardcastle & Worrall 2000; Hardcastle et al. 2006), but the spectral property is still uncertain, especially for FR-I radio galaxies, due to the contribution of the accretion disk.

Centaurus A (Cen A) is the nearest radio galaxy, and its gamma-ray emission has been established by *Fermi* (Abdo et al. 2009a, 2010c) and H.E.S.S. (Aharonian et al. 2009), it is the second-brightest GeV gamma-ray radio galaxy, following NGC 1275 (Abdo et al. 2009b, 2010b). The GeV gamma-ray emission does not come from the kiloparsec-scale jet but likely from the beamed sub-arcsecond jet resolved by very long baseline interferometry (Abdo et al. 2010c; Müller et al. 2011). In addition, *Fermi* found that sub-Mpc giant radio lobes of Cen A are also GeV gamma-ray emitters (Abdo et al. 2010d). Nonthermal soft X-ray emission from the sub-arcsecond jet is suggested for Cen A (Evans et al. 2004). On the other hand, *Chandra* resolved the X-ray emission from kiloparsec-scale jets (Kraft et al. 2000). Cen A is the brightest active galactic nucleus (AGN) in the hard X-ray band (Tueller et al. 2008), and the X-ray spectrum is very similar to that of Seyfert galaxies (Wang et al. 1986; Kinzer et al. 1995; Rothschild et al. 1999). On the other hand, it seems to smoothly connect to the MeV/GeV emission detected with *Compton Gamma Ray Observatory* (*CGRO*) COMPTEL/EGRET, such as blazars (Steinle et al. 1998; Sreekumar et al. 1999). *Suzaku* observed Cen A in 2005, and it was reported that Seyfert-like X-ray emission was dominated (Markowitz et al. 2007). Based on the *International Gamma-Ray Astrophysics Laboratory* (*INTEGRAL*) time-averaged spectra with a long exposure, Beckmann et al. (2011) also indicated that the origin of the hard X-rays was thought to be a Seyfert-like emission but the nonthermal emission scenario cannot be ruled out. Another finding on the Cen A X-ray spectrum is that the reflection continuum was often not required in the spectral fitting (Rothschild et al. 1999, 2011; Markowitz et al. 2007; Beckmann et al. 2011), regardless of the existence of a neutral Fe–K fluorescence line. Therefore, interpretation of the Cen A X-ray spectrum still has several open issues.

However, detailed studies of spectral variation in the hard X-ray band have not been reported yet. Time variability of X-ray spectra gives us important opportunities to decompose the spectral components. The Cen A spectrum is strongly absorbed in the soft X-ray band like Seyfert 2 galaxies, and therefore the study of the hard X-ray time variation is important. In order to measure the spectral variability in detail, we again observed Cen A with *Suzaku*, which enables us to measure the short-term time variation in the hard X-ray band with the best accuracy. In this paper, we report the studies of X-ray spectral variability of Cen A with *Suzaku* (Mitsuda et al. 2007). Throughout this paper, we assumed the distance to Cen A to be 3.8 Mpc (Rejkuba 2004), and the errors are shown as a 90% confidence level. We refer to

Table 1
Summary of *Suzaku* Observations of Cen A

ObsID	Date	Start	Stop	Exposure[a]
100005010	2005 Aug 19–20	08–19 03:39:19	08–20 09:50:08	37984
704018010	2009 Jul 20–21	07–20 08:55:29	07–21 18:26:24	44587
704018020	2009 Aug 5–6	08–05 07:23:27	08–06 16:52:14	35093
704018030	2009 Aug 14–16	08–14 09:06:56	08–16 02:31:24	37636

Note. [a] Exposure time of the HXD-PIN data after data reduction.

the solar photospheric values (Anders & Grevesse 1989) for the solar abundance ratio of the photoelectric absorption, reflection, and plasma model. The cross section for absorption models is set to that of Balucińska-Church & McCammon (1992).

2. OBSERVATION AND DATA REDUCTION

We observed Cen A three times with *Suzaku* in 2009 July 20–21, August 5–6, and August 14–16, as summarized in Table 1. In this paper, we also analyzed the *Suzaku* data obtained in 2005 in the same way for comparison. Figure 1 shows the periods of *Suzaku* observations on the *Swift*/BAT light curve.[1] Cen A entered an active phase beginning in the summer of 2007. The 2005 data correspond to the low state, while the 2009 data correspond to the high state. All the observations were performed with X-ray Imaging Spectrometer (XIS) 5 × 5 or 3 × 3 modes (Koyama et al. 2007) and a normal Hard X-ray Detector (HXD) mode (Takahashi et al. 2007; Kokubun et al. 2007), except for the XIS observation in 2005, which was operated in 5 × 5, 3 × 3, or 2 × 2 modes with a 1/4 window option in order to avoid a pile-up. The Cen A was observed at the XIS nominal position in 2005, while it was observed at the HXD nominal position in 2009. The XIS count rate was 7–10 counts s^{-1} in 2009, and thus a pile-up did not occur. We also confirmed no pile-up effects by checking that the results of the spectral fittings did not change when we excluded the central 2 arcmin region.

We utilized the data processed with the *Suzaku* version 2.4 pipeline software and performed the standard data reduction with criteria such as a pointing difference of $<1\overset{\circ}{.}5$, an elevation angle of $>5^{\circ}$ from the Earth rim, a geomagnetic cutoff rigidity (COR) of >6 GV, and the South Atlantic Anomaly (SAA)-elapsed time of >256 s. Further selection was applied with criteria such as an Earth elevation angle of $>20^{\circ}$ for XIS, COR > 8 GV, and the SAA-elapsed time (T_SAA_HXD) of >500 s for HXD. XIS photon events were accumulated within 4 arcmin of the Cen A nucleus, with the XIS- 0, 2, and 3 data coadded. The XIS rmf and arf files were created with `xisrmfgen` and `xisarfgen` (Ishisaki et al. 2007), respectively, and the XIS detector background was estimated with `xisnxbgen` (Tawa et al. 2008). For HXD, the "tuned" PIN and GSO background was used (Fukazawa et al. 2009) and the good time interval (GTI) was determined by taking the logical-end of GTIs among the data and background model. Since the XIS light-leakage estimation was not valid at the beginning of the 2005 observation, we eliminated the data in the first 12 hr. Note that Markowitz et al. (2007) included this period in the analysis and therefore our results are somewhat different from theirs for absorption model parameters and so on. For XIS and HXD-PIN, Cosmic X-ray Background (CXB) was added to the background spectrum thus obtained, although it is negligible for the HXD-GSO. The latest GSO response file (version 20100524) and the GSO response correction file (version 20100526) were utilized. The former is updated in terms of energy-channel linearity and GSO gain history (Yamada et al. 2011), and the latter compensated for any disagreement of 10%–20% between the Crab spectral model and the data.[2]

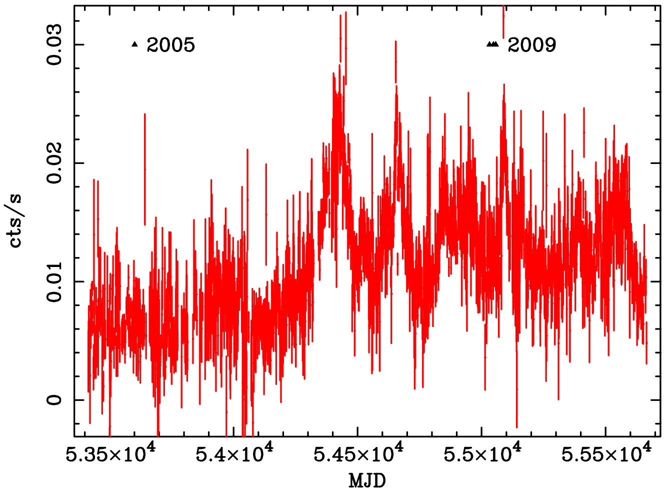

Figure 1. *Swift*/BAT light curve of the Cen A in the 15–50 keV band. Triangles represent the period of *Suzaku* observations.

(A color version of this figure is available in the online journal.)

As a result, a net exposure time for XIS is around 33 ks, 62 ks, 51 ks, and 56 ks for the 2005, 2009 first, second, and third observations, respectively. The exposure time for HXD is about 70% of the XIS ones, due to additional cuts of high background periods. The HXD-PIN signal rate is higher than the background rate below 50 keV, while the HXD-GSO signal rate is <10% of the background rate. Therefore, we checked the reproducibility of the GSO background as described in the Appendix. As a result, the reproducibility of the GSO background is found to be as good as around 1%. Note that the data of the 2009 first observation were already used in Abdo et al. (2010c).

3. DATA ANALYSIS

3.1. Light Curves and Correlations

Figure 2 shows the count-rate light curves of XIS (3–8 keV), PIN (15–40 keV), and GSO (50–100 keV), with a time bin of 10 ks. The background was subtracted for PIN and GSO, while the XIS background rate is <1% of the signal, and thus is negligible. Note that the background rate of PIN and GSO is around 0.3 and 8–10 counts s^{-1}, respectively. All the observations clearly exhibit time variability in the XIS and PIN light curves with an amplitude of up to 50% and a timescale of 10–20 ks. This timescale is reasonable for the black hole mass of $(0.5–1) \sim 10^{8} M_{\odot}$ (Silge et al. 2005; Krajnović et al. 2007; Neumayer et al. 2007). The largest variability occurred during the first observation of 2009. Looking at the light curves, there is a different variability pattern between XIS and PIN. For example, at 0–50,000 s (1st–5th bin) in the first observation of 2009, the rising trend of the count rate is linear for PIN and concave for XIS. At 0–70,000 s (29–35th bin) in the 2009 third observation, the variability pattern is also different between XIS

---

[1] http://swift.gsfc.nasa.gov/docs/swift/results/transients/

[2] http://www.astro.isas.jaxa.jp/suzaku/analysis/hxd/gsoarf2/

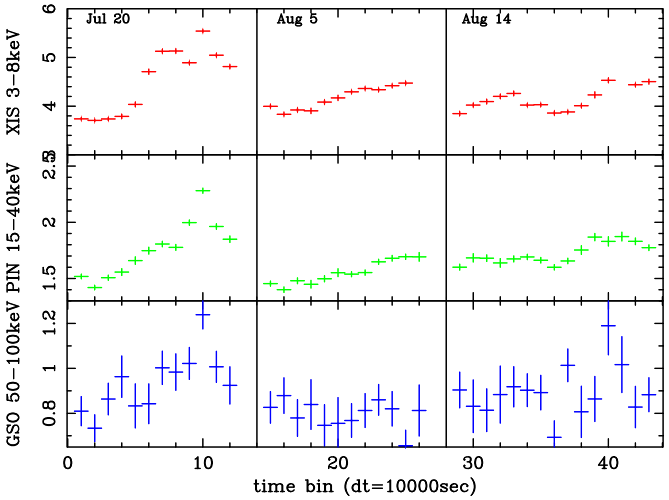

Figure 2. *Suzaku* light curve of Cen A for the 2009 *Suzaku* observations. From top to bottom, XIS-F (3–8 keV), PIN (15–40 keV), and GSO (50–100 keV) are presented. The horizontal axis indicates the time bin number with a step of 10,000 s. The beginning of the light curves is 55032.328958, 55048.284699, and 55057.380162 in MJD, for the first, second, and third observations, respectively.

(A color version of this figure is available in the online journal.)

and PIN. For the GSO light curve, the error is somewhat large, but a similar trend of variability is clearly seen.

Figure 3 shows a correlation of the count rate among different energy bands. We do not treat the 2005 data, since the XIS-to-PIN effective area ratio is different between 2005 and 2009 and the data duration of the 2005 observation was short. The XIS count rate in 3–8 keV generally correlates with the PIN count rate in 15–40 keV, but the slope is different among observations. Furthermore, the correlation is not completely linear, especially for the 2009 first and third observations; the deviation is up to 20% or so. These trends indicate that the spectral shape varied significantly, suggesting multiple spectral components or a change of the spectral shape. On the other hand, considering that the GSO background reproducibility is around 0.1–0.2 counts s^{-1} (Fukazawa et al. 2009), it can be said that the GSO count rate in 50–100 keV correlates with the PIN count rate within 10%–20%. This situation is also the same as that in 100–200 keV. Therefore, the emission in 15–200 keV could be mainly explained by a combination of a variable component and a constant component within errors.

3.2. Modeling of the Soft X-Ray Component

The X-ray spectrum of Cen A is known to consist of roughly two components: a spatially extended component in the soft band and a strongly absorbed hard nuclear component (Markowitz et al. 2007). The former extended component was clearly resolved into many complex features associated with the Cen A jets, such as kiloparsec-jets and shock regions, together with interstellar hot medium and discrete sources in the parent galaxy (Kraft et al. 2008). Notably, shock regions show a relatively hard power-law emission (Croston et al. 2009), whose flux is lower by two orders of magnitude than that of the nuclear X-ray emission. Since the spectral component in the soft band somewhat affects the modeling of the nuclear component, we first modeled the soft component by using the XIS data of the second observation of 2009. Before this analysis, we fitted the XIS spectra in 2–10 keV to model the hard X-ray continuum with the absorbed power-law model. Then, we included the model of the hard component whose parameters are fixed to the values

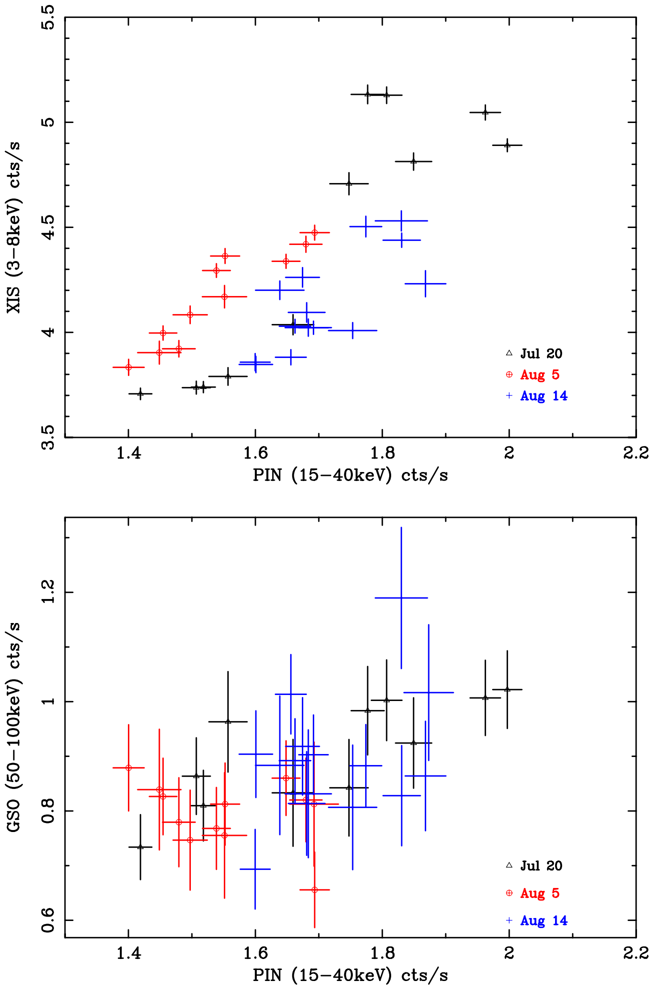

Figure 3. Correlation of count rates of XIS (3–8 keV, left) and GSO (50–100 keV, right) against PIN (15–40 keV). The triangles, circles, and crosses are the data of the first, second, and third observations in 2009.

(A color version of this figure is available in the online journal.)

obtained above, except for the power-law normalization, and fitted the XIS spectra in 0.7–3 keV with an APEC thermal plasma model together with the absorbed power-law model. The metal abundance is left free, and the photoelectric absorption model PHABS is multiplied. The relative normalization between XIS-F and XIS-B is let free, due to calibration uncertainties associated with attitude fluctuations. We ignored the 1.82–1.84 keV band due to the XIS calibration problems. However, this modeling could not reproduce the spectra with a reduced χ^2 value of 4.14, since the APEC model cannot simultaneously explain the emission lines and the continuum around 1.5–2 keV where the spectral slope is around 2. Next, we added the BREMSS model with the absorption to model the extended hard emission from unresolved point sources and jet features in Cen A (Matsushita et al. 1994). Many sources in Cen A could contribute to the X-ray emission, but the obtained X-ray luminosity of the BREMSS component is 8×10^{39} erg s^{-1} (2–10 keV), which can be explained by the sum of X-ray point sources in Cen A (Kraft et al. 2001). This is not a concern of this paper, and we do not discuss it further. This model improved the fit, and a reduced χ^2 value became 1.44, but the emission lines could not be reproduced well. Markowitz et al. (2007) reported that two-temperature plasma components were required.

Table 2
Fitting Results of the XIS Soft Thermal Components

Obs	$I_{\rm bremss}$[a] (10^{-3})	kT_1 (keV)	$I_{\rm apec1}$[b] (10^{-3})	kT_2 (keV)	$I_{\rm apec2}$[c] (10^{-3})	χ^2/dof (χ^2, dof)
2005	1.5 ± 0.1	0.71 ± 0.02	1.7 ± 0.3	0.32 ± 0.01	3.9 ± 0.8	2.02 (616.8/306)
2009a	1.6 ± 0.1	0.72 ± 0.03	1.8 ± 0.4	0.33 ± 0.03	3.8 ± 1.2	1.49 (455.2/306)
2009b	1.8 ± 0.1	0.79 ± 0.05	1.6 ± 0.5	0.29 ± 0.01	5.3 ± 0.5	1.25 (389.9/313)
2009c	1.7 ± 0.1	0.72 ± 0.04	2.0 ± 0.5	0.28 ± 0.02	4.9 ± 1.5	1.30 (398.2/306)
Adapted values[d]	...	0.72	...	0.30	4.0	...

Notes. Two APEC models are multiplied by the photoelectric absorption, whose absorption column density is fixed to 1.6×10^{21} cm^{-2}. Metal abundances of both APEC models are fixed to 0.3 solar. A temperature of the bremsstrahlung is fixed at 7 keV.

[a] Normalization of the bremsstrahlung.

[b] Normalization of the APEC model 1.

[c] Normalization of the APEC model 2.

[d] Adapted values of spectral parameters for fitting the wide-band *Suzaku* spectra.

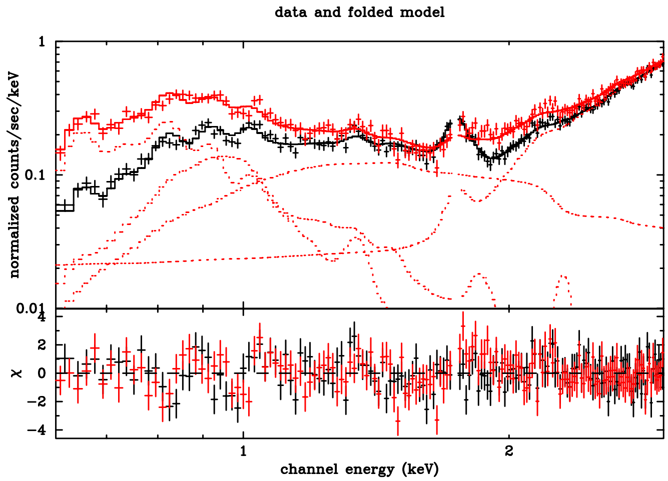

Figure 4. Spectral fitting of the XIS spectra in the second observation of 2009 with the two-temperature APEC plasma models plus bremsstrahlung, together with the emission model of the nuclear emission seen above 2 keV. Details are described in the text. The solid line represents the best-fit total emission model, and the dotted lines represent each spectral component: two APEC, a BREMSS, and an absorbed power law. The red and black ones correspond to XIS-B and XIS-F, respectively.

(A color version of this figure is available in the online journal.)

We thus added one more APEC model whose temperature and abundance were left free. Then, the spectrum was well fitted with the best-fit absorption column density and metal abundance of 1.6×10^{21} cm^{-2} and ∼0.3 solar, respectively, but their errors became larger. The former best-fit value is somewhat larger than that of the Galactic value 8.6×10^{20} cm^{-2} (Dickey & Lockman 1990), implying an additional intrinsic absorber, such as interstellar medium, within the parent galaxy. We hereafter fixed the absorption column density and metal abundance to the above values. Evans et al. (2004) and Markowitz et al. (2007) reported the detection of Si and S fluorescence lines. In this analysis, the Si–K line is not significant with an upper limit of 7×10^{-6} counts s^{-1} cm^{-2}. Therefore, we include the S–K line at 2.306 keV in the model, which then improved the fit with $\Delta\chi^2 = 10$, and its intensity is $1.57^{+0.70}_{-0.97} \times 10^{-5}$ counts s^{-1} cm^{-2}. As a result, the soft X-ray spectra could be fitted well with a reduced χ^2 value of 1.25, as shown in Figure 4 and the best-fit parameters are summarized in Table 2.

We also analyzed the XIS spectra of other observations in the same way as above, and the results are summarized in Table 2. Since the thermal components are believed to be extended, their parameters should be constant and the best-fit values are consistent among all the observations within errors. In the following broadband fitting for all the observations, we fixed the temperatures and column densities of the above model to the values in Table 2.

3.3. Time-averaged Spectrum of Each Observation

Although the spectral variability during each observation is indicated in the previous subsection, we analyze here the time-averaged spectrum of each observation in order to understand the spectral shape. At first, we describe the spectral fitting of the second observation of 2009, whose time variability was relatively moderate. After determining the best-fit modeling, we apply it to other observations.

We then fit the XIS-F, XIS-B, PIN, and GSO spectra of the second observation of 2009 in 0.7–300 keV simultaneously to model the nuclear hard component. For each detector, the energy ranges of 0.7–10 keV, 15–70 keV, and 55–300 keV for XIS, PIN, and GSO, respectively, are used in the fitting. A relative normalization between XIS-F and XIS-B is left to be free, while that between XIS and PIN, or between PIN and GSO, is fixed at 1.18 (Maeda et al. 2008) or 1.0,[3] respectively. The spectral models for the soft X-ray emission were included, but the model parameters of two APEC models and the BREMSS model are fixed, and normalizations of the higher-temperature APEC model and the BREMSS model are left free.

For the hard nuclear component, we at first tried the basic model: an absorbed power law with an Fe–K line (model A). For the strong photoelectric absorption of nuclear emission, we use the ZVPHABS model, where the Fe abundance is left free and other elemental abundances are fixed to one solar. We tentatively included the high energy cutoff fixed at 1000 keV for the power-law model. The broadband X-ray spectra in 0.7–300 keV are overall fitted with this basic model. The residual of fitting with this model is shown in the first panel of Figure 5, where a reduced χ^2 value is 1.21. However, significant residual structures are seen around 15–30 keV and 50–300 keV. The residual around 15–30 keV could be due to the reflection component, so we then included the PEXRAV model (Zdziarski et al. 1995) for the reflection (model B), where the input power-law parameters of the PEXRAV model are tied to those of the direct nuclear power-law model and the inclination angle is assumed to be

---

[3] http://www.astro.isas.jaxa.jp/suzaku/analysis/hxd/gsoarf2/

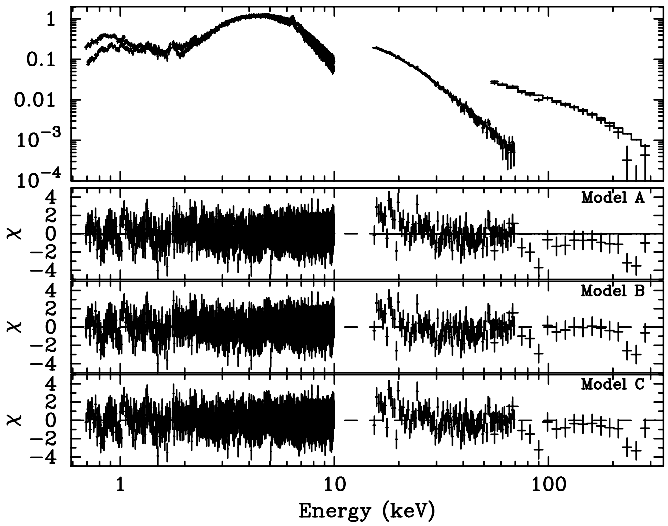

Figure 5. Spectral fitting of the XIS/PIN/GSO spectra in the second observation of 2009 with models A, B, and C. A detailed description of the models is described in the text. The top panel shows the XIS/PIN/GSO spectra with best-fit model C. The second, third, and fourth panels show the residual of the fitting for models A, B, and C, respectively.

$\cos\theta = 0.5$ ($\theta = 60°$); only the free parameter is the reflection fraction R. Furthermore, we multiplied the reflection component by the absorption. As shown in the second panel of Figure 5, the residual around 15–40 keV still slightly remains, but the fit improved with $\Delta\chi^2 = 35$ with the addition of two parameters. The reflection fraction became $R = 0.19$, while the absorption of the reflection component is not required.

Alternatively, the residual structure in the first panel of Figure 5 could be reproduced by a partial covering absorption with a column density of $\sim 10^{24}$ cm^{-2}. Then, instead of the reflection, we included the PCFABS model for representing the partial covering absorption (model C). The fit gave a similar χ^2 value (the difference of χ^2 is 13) to that for model B (the third and fourth panels in Figure 5). The best-fit model gave a column density of $(2.7 \pm 1.1) \times 10^{23}$ cm^{-2} and a covering fraction of 9% ± 3% for the partial covering absorber.

We applied the above models to other observations. Since the observational detector position of Cen A is different between 2005 and 2009, a relative normalization between XIS and PIN is different. Unlike 2009, the position of the 2005 observation is not nominal, and thus a nominal relative ratio of normalizations is not available. Therefore, we at first set a relative normalization between XIS and PIN to be free, and obtained it to be 1.06. This is consistent with the value in Markowitz et al. (2007). Accordingly, we hereafter fixed the relative normalization to 1.06 for the 2005 observation.

The fitting results of the four observations for models A, B, and C are summarized in Tables 3–5. Models B and C provided a better fit than the model A for all the observations, and they gave

Table 3

Results of Simultaneous Fitting of the XIS/PIN/GSO Spectra (Model A)

Parameters	Unit	2005	2009a	2009b	2009c
$N_{\rm H}$[a]	(10^{23})	1.20 ± 0.01	0.93 ± 0.01	1.03 ± 0.01	1.04 ± 0.01
$A_{\rm Fe}$[b]	(Solar)	0.65 ± 0.05	1.53 ± 0.06	1.10 ± 0.07	1.09 ± 0.06
$\alpha_{\rm ph}$[c]		1.82 ± 0.05	1.64 ± 0.05	1.68 ± 0.06	1.67 ± 0.05
$I_{\rm pow}$[d]		0.117 ± 0.003	0.117 ± 0.003	0.117 ± 0.003	0.126 ± 0.003
$E_{\rm Fe}$[e]	(keV)	6.398 ± 0.004	6.392 ± 0.006	6.394 ± 0.007	6.395 ± 0.008
$I_{\rm Fe}$[f]	(10^{-4})	2.6 ± 0.2	2.6 ± 0.3	3.0 ± 0.3	2.7 ± 0.3
χ^2/dof		1.85	1.50	1.14	1.31
(χ^2, dof)		(2314.7/1248)	(2093.4/1392)	(1539.8/1353)	(1796.7/1369)

Notes. Model A is `constant*phabs*([highecut*zvphabs*powerlaw + zgauss] + apec + apec + phabs*bremss + zgauss)` in XSPEC. Components between parentheses [ ] represent the AGN emission.

[a,b] Hydrogen column density and Fe abundance of the absorber. The column density is in unit of cm^{-2} for the ZVPHABS model.

[c,d] Photon index and normalization at 1 keV of the power-law model.

[e,f] Center energy and normalization of the Fe–Kα line. The normalization is in unit of photons cm^{-2} s^{-1}.

Table 4

Results of Simultaneous Fitting of the XIS/PIN/GSO Spectra (Model B)

Parameters	Unit	2005	2009a	2009b	2009c
$N_{\rm H}$[a]	(10^{23})	1.25 ± 0.01	1.01 ± 0.01	1.07 ± 0.01	1.08 ± 0.01
$A_{\rm Fe}$[b]	(Solar)	0.46 ± 0.03	1.14 ± 0.05	0.94 ± 0.06	0.86 ± 0.07
$\alpha_{\rm ph}$[c]		1.90 ± 0.05	1.73 ± 0.05	1.73 ± 0.06	1.72 ± 0.06
$I_{\rm pow}$[d]		0.127 ± 0.003	0.132 ± 0.003	0.126 ± 0.004	0.131 ± 0.004
$E_{\rm Fe}$[e]	(keV)	6.398 ± 0.004	6.391 ± 0.006	6.396 ± 0.006	6.396 ± 0.007
$I_{\rm Fe}$[f]	(10^{-4})	2.7 ± 0.2	2.7 ± 0.3	3.1 ± 0.3	2.8 ± 0.3
R[g]	($\Omega/2\pi$)	0.406 ± 0.002	0.345 ± 0.003	0.192 ± 0.004	0.220 ± 0.005
χ^2/dof		1.71	1.42	1.11	1.23
(χ^2, dof)		(2129.7/1246)	(1968.6/1390)	(1505.0/1351)	(1683.6/1367)

Notes. Model B is `constant*phabs*([highecut*zvphabs*powerlaw + zgauss + phabs*pexrav] + apec + apec + phabs*bremss + zgauss)` in XSPEC. Components between parentheses [ ] represent the AGN emission.

[a,b] Hydrogen column density and Fe abundance of the absorber. The column density is in units of cm^{-2} for the ZVPHABS model.

[c,d] Photon index and normalization at 1 keV of the power-law model.

[e,f] Center energy and normalization of the Fe–Kα line. The normalization is in units of photons cm^{-2} s^{-1}.

[g] Fraction of the reflection component for the PEXRAV model.

Table 5
Results of Simultaneous Fitting of the XIS/PIN/GSO Spectra (Model C)

Parameters	Unit	2005	2009a	2009b	2009c
N_{H}[a]	(10^{23})	1.17 ± 0.04	0.97 ± 0.03	1.01 ± 0.03	1.05 ± 0.04
A_{Fe}[b]	(Solar)	0.51 ± 0.10	1.33 ± 0.11	1.11 ± 0.08	0.93 ± 0.11
α_{ph}[c]		1.94 ± 0.46	1.68 ± 0.30	1.71 ± 0.31	1.69 ± 0.43
I_{pow}[d]		0.176 ± 0.040	0.138 ± 0.021	0.129 ± 0.020	0.138 ± 0.029
E_{Fe}[e]	(keV)	6.398 ± 0.005	6.392 ± 0.006	6.395 ± 0.007	6.396 ± 0.007
I_{Fe}[f]	(10^{-4})	2.3 ± 0.2	2.7 ± 0.3	2.9 ± 0.3	2.8 ± 0.3
$N_{\mathrm{H,2}}$[g]	(10^{24})	0.41 ± 0.04	1.58 ± 0.33	0.27 ± 0.11	1.10 ± 0.27
f_{NH2}[h]		0.29 ± 0.03	0.10 ± 0.02	0.09 ± 0.03	0.08 ± 0.03
χ^2/dof		1.43	1.42	1.11	1.23
(χ^2, dof)		(1783.8/1245)	(1970.6/1390)	(1494.2/1351)	(1677.6/1367)

Notes. Model C is `constant*phabs*([pcfabs*highecut*zvphabs*powerlaw + zgauss] + apec + apec + phabs*bremss + zgauss)` in XSPEC. Components between parentheses [ ] represent the AGN emission.

[a,b] Hydrogen column density and Fe abundance of the absorber. The column density is in units of cm^{-2} for the ZVPHABS model.

[c,d] Photon index and normalization at 1 keV of the power-law model.

[e,f] Center energy and normalization of the Fe–Kα line. The normalization is in units of photons $\mathrm{cm}^{-2}\ \mathrm{s}^{-1}$.

[g,h] Hydrogen column density and covering fraction of the absorber for the PCFABS model.

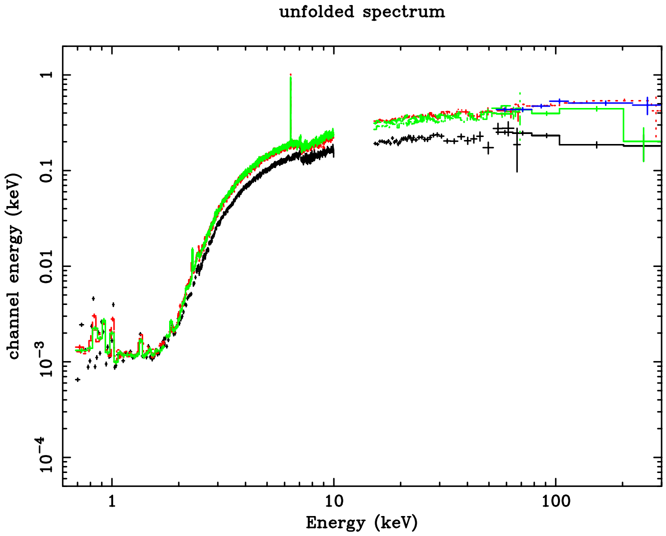

Figure 6. $\nu F \nu$ plots of the XIS/PIN/GSO spectra for all observations. Black, red, green, and blue data correspond to the spectrum of the 2005, first 2009, second 2009, and third 2009 observations, respectively.

(A color version of this figure is available in the online journal.)

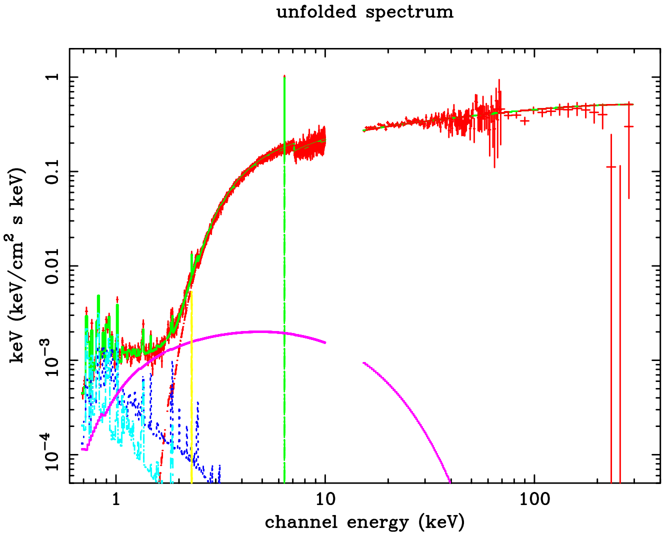

Figure 7. $\nu F \nu$ plots of the XIS/PIN/GSO spectra with model C for the second observation of 2009.

(A color version of this figure is available in the online journal.)

a similar χ^2 value for the three 2009 observations, while model C provided a significant improvement of the fitting for the 2005 observation. Markowitz et al. (2007) reported a similar trend for the 2005 observation. Figure 6 compares the $\nu F \nu$ spectra of all observations, and Figure 7 shows the best-fit $\nu F \nu$ spectra of the second observation of 2009. It can be seen that the soft X-ray emission in 0.7–2 keV is at almost the same flux level, because the emission comes from the extended region while the hard X-ray emission brightened in 2009; 0.2 keV $\mathrm{cm}^{-2}\ \mathrm{s}^{-1}$ and 0.2 keV $\mathrm{cm}^{-2}\ \mathrm{s}^{-1}$ at 20 keV and 100 keV, respectively, in 2005, 0.3–0.4 keV $\mathrm{cm}^{-2}\ \mathrm{s}^{-1}$ and 0.4–0.5 keV $\mathrm{cm}^{-2}\ \mathrm{s}^{-1}$ at 20 keV and 100 keV, respectively, in 2009. In the following, let us look at the fitting results for model C. The column density of the uniform absorber is almost constant at $1.0 \times 10^{23}\ \mathrm{cm}^{-2}$ for all the observations. The covering fraction of the partial covering absorber is around 30% in 2005, while it is around 8%–10% in 2009. The column density of the partial covering absorber is not constant, but two observations in 2009 gave a Compton-thick value of $> 10^{24}\ \mathrm{cm}^{-2}$. The large difference appears for the power-law photon index; 1.94 in 2005 and 1.68–1.71 in 2009. In other words, the Cen A spectrum became significantly harder in 2009 as can be seen in Figure 7. The intensity of the neutral Fe–K fluorescence line is $(2.3 \pm 0.2) \times 10^{-4}$ counts $\mathrm{s}^{-1}\ \mathrm{cm}^{-2}$ in 2005 and $(2.7–2.9) \times 10^{-4}$ counts $\mathrm{s}^{-1}\ \mathrm{cm}^{-2}$ in 2009. This is the first evidence of variability for the Fe–K line intensity for the Cen A, and the Fe–K line intensity is considered to be high in 2009 as a result of brightening of the Cen A continuum emission since 2007.

Although the time-averaged spectra can be fitted with models B or C, both of the models have problems. For model B, the reflection component is generally considered to be constant and thus only the power-law component cannot explain the complex time variability as described in Section 3.1. The fluorescence Fe–K line is significantly detected with an equivalent width (EW) of 78, 56, 69, and 56 eV for the 2005 observation and the first, second, and third observations of 2009, respectively, indicating that there is an underlying reflection continuum and thus model C does not match this evidence. The reflection fraction in model B is around 0.19–0.34 in 2009 and 0.41 in 2005. The EW of the Fe–K line against the reflection component

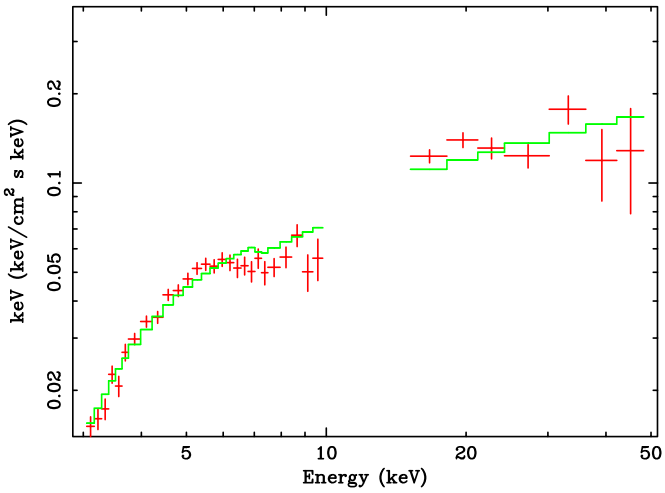

Figure 8. $\nu F \nu$ plots of the difference spectra of XIS/PIN between high and low periods in the first observation of 2009. The solid line represents a power-law model with a simple absorption.

(A color version of this figure is available in the online journal.)

is 1.0–2.0 keV, which is reasonable for the Compton-thick reflector with one solar abundance. Therefore, both the reflection component and the partial covering absorption are likely to be required.

The above results are obtained by assuming that the exponential cutoff energy of the power-law model is 1000 keV. Then, we let it free for model C, but only a lower limit of ∼500 keV is obtained both in 2005 and 2009. Therefore, hereafter, we fixed the cutoff energy to 1000 keV.

3.4. Difference Spectra between High and Low Flux Periods

Before performing the spectral fitting by including both the reflection and the partial covering absorption, it is important to study the spectral component which produces the complex time variability. Here, we investigated the difference spectra between high and low flux periods in 2009 observations. We used the XIS-F and HXD-PIN data for this analysis, since XIS-B and HXD-GSO did not give an enough signal-to-noise ratio for this analysis.

First, we took a different spectrum between high and low flux periods in each observation. We defined high and low flux periods in Figure 2 as follows: the bins 8–11, bins 22–24, and bins 39–42 for high flux periods, and the bins 1–4, bins 15–17, and bins 29–32 for low flux periods. We fitted the difference spectra defined as above with an absorbed power-law model, which typically represents the difference spectra of Seyfert galaxies (e.g., Miniutti et al. 2007; Shirai et al. 2008). Figure 8 shows the fitting results for the first observation. The overall spectral shape is represented by the absorbed power-law model, but the fit is not good with a reduced χ^2 value of 2.33. There is a strong Fe–K edge feature in the observed spectrum and it is not reproduced well by the best-fit model. This indicates a thicker absorber, and thus we tried a partial covering absorption model. Then, the fit improved with $\Delta\chi^2 = 36$, and the edge feature can be fitted with this model. Figure 9 shows a confidence contour between the partial covering fraction and the photon index. The Compton-thick absorber of $N_{\rm H} = 2.6 \times 10^{24}$ cm^{-2} with a high covering fraction of 0.64 is required by the deep Fe–K edge structure. The power-law photon index is 2.23 ± 0.18, somewhat steeper than the index for the time-averaged spectra.

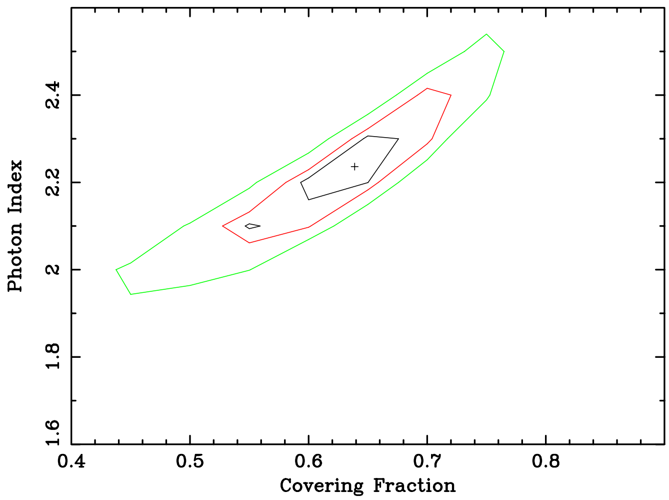

Figure 9. Confidence contour between the partial covering fraction of absorption and the power-law photon index.

(A color version of this figure is available in the online journal.)

For the other two observations, since the signal-to-noise ratio of spectra is not high, the Fe–K edge feature is less clear. However, when the spectra are fitted by a power-law model with a simple absorption, the photon index becomes very small; 1.4 ± 0.2 and 1.2 ± 0.2 for the second and third observations, respectively. When the partial covering absorption model is introduced, the power-law photon index becomes reasonable around 2 for the second observation. This is not the case for the third observation; errors of photon index and absorption column density are large. When we fixed the photon index to 2.0 for the third observation, the absorption column density of the uniform absorber becomes reasonable around 1×10^{23} cm^{-2}. The fitting results are summarized in Table 6. The partial absorber has a large column density of $>10^{24}$ cm^{-2} with a large covering fraction of >0.3, and they seem variable. These behaviors could cause a complex time variability. Such a Compton-thick absorber was observed for the first time for Cen A.

The partial covering absorber is thought to be variable during each observation. Therefore, we investigated a spectral variability with a finer time resolution. We divided one observation into several periods with a step of 10 ks, following the light curve in Figure 2, and took a different spectrum between two periods, one of which is the low flux period just before brightening and the other is around the highest flux level. We took the difference between bins 7 and 3 during the first observation, bins 10 and 9 during the first observation, bins 24 and 16 during the second observation, and bins 41 and 38 during the third observation in Figure 2. Table 6 summarized the fitting results of the partial covering absorption model with the photon index fixed to 2.0. Since the signal-to-noise ratio of each spectrum is not so high, errors are large. However, the column density and covering fraction are not constant while the column density of the uniform absorber is constant around 1×10^{23} cm^{-2}.

In summary, the complex time variability of Cen A is likely to be caused by the variability of the partial covering absorber with a timescale of $<$10,000 s, while the power-law photon index is almost stable around 2.0.

3.5. Additional Hard Power-law Component

Since the partial covering absorber was found to exist through studying spectral variability, both the reflection and the partial

Table 6
Results of Spectral Fitting of the XIS/PIN Difference Spectra with a Power-law Model with a Partial Covering Absorption

Observation	Unit	N_{H1} [a] 10^{22}	α [b]	N_{H2} [c] 10^{24}	f_{NH2} [d]
2009 first	High–Low	13.2 ± 1.3	2.23 ± 0.18	2.67 ± 0.98	0.64 ± 0.09
2009 second	High–Low	11.7 ± 6.5	2.08 ± 0.81	>1.00	0.65 ± 0.43
2009 third	High–Low	11.6 ± 0.7	2 (fix)	>0.51	0.72 ± 0.17
2009 first	7–3th	13.6 ± 2.1	2 (fix)	>0.57	0.29 ± 0.21
2009 first	10–9th	12(fix)	2 (fix)	>1.19	0.64 ± 0.15
2009 second	24–16th	11.4 ± 3.0	2 (fix)	>1.31	0.71 ± 0.13
2009 third	41–38th	12(fix)	2 (fix)	>0.03	0.60 ± 0.25

Notes.
[a] Hydrogen column density of the uniform absorber in units of cm^{-2}.
[b] Photon index and normalization at 1 keV of the power-law model.
[c,d] Hydrogen column density and covering fraction of the absorber for the PCFABS model.

Table 7
Results of Simultaneous Fitting of the XIS/PIN/GSO Spectra (Model D)

Parameters	Unit	2005	2009a	2009b	2009c
N_{H} [a]	(10^{23})	1.17 ± 0.03	1.01 ± 0.01	1.07 ± 0.02	1.08 ± 0.01
A_{Fe} [b]	(Solar)	0.50 ± 0.10	1.13 ± 0.05	0.92 ± 0.07	0.83 ± 0.07
α_{ph} [c]		1.96 ± 0.42	1.73 ± 0.05	1.73 ± 0.12	1.71 ± 0.07
I_{pow} [d]		0.169 ± 0.035	0.134 ± 0.003	0.128 ± 0.007	0.133 ± 0.004
E_{Fe} [e]	(keV)	6.397 ± 0.004	6.391 ± 0.006	6.396 ± 0.007	6.396 ± 0.007
I_{Fe} [f]	(10^{-4})	2.4 ± 0.2	2.7 ± 0.3	3.0 ± 0.3	2.8 ± 0.3
$N_{\mathrm{H,2}}$ [g]	(10^{24})	0.33 ± 0.04	1.64 ± 1.08	0.34 ± 0.29	0.98 ± 0.68
f_{NH2} [h]		0.26 ± 0.03	<0.05	<0.05	<0.03
R [i]	$(\Omega/2\pi)$	0.236 ± 0.002	0.304 ± 0.003	0.147 ± 0.005	0.183 ± 0.004
χ^2/dof		1.43	1.41	1.11	1.23
(χ^2, dof)		(1773.7/1243)	(1962.7/1388)	(1495.2/1349)	(1678.7/1365)

Notes. Model D is `constant*phabs*([pcfabs*highecut*zvphabs*powerlaw + zgauss + phabs*pexrav] + apec + apec + phabs*bremss + zgauss)` in XSPEC. Components between parentheses [ ] represent the AGN emission.
[a,b] Hydrogen column density and Fe abundance of the absorber. The column density is in units of cm^{-2} for the ZVPHABS model.
[c,d] Photon index and normalization at 1 keV of the power-law model.
[e,f] Center energy and normalization of the Fe–Kα line. The normalization is in units of photons $\mathrm{cm}^{-2}\ \mathrm{s}^{-1}$.
[g,h] Hydrogen column density and covering fraction of the absorber for the PCFABS model.
[i] Fraction of the reflection component for the PEXRAV model.

covering absorber need to fit the *Suzaku* wide-band X-ray spectra of Cen A. Then, we fitted the time-averaged spectrum of each observation by considering both spectral features (model D). The fitting results are summarized in Table 7. The reduced χ^2 is almost the same as that of model C (partial covering absorption without reflection), and the reflection continuum is not required. This is inconsistent with the existence of the Fe–K line. Another problem is that the power-law photon index of 1.7 for the time-averaged spectra in 2009 is different from that obtained by the analysis of difference spectra, which require a photon index of $\sim$2.

The power-law component is generally thought to be due to the thermal Comptonization of disk photons, as well as the low/hard state of black hole binaries. When Cyg X-1 and GX 339-4 are brighter in the low/hard state, the Compton thickness becomes larger but the Comptonizing electron temperature decreases (Makishima et al. 2008; Zdziarski et al. 2004; Del Santo et al. 2008). As a result, the power-law photon index and cutoff energy are larger and lower, respectively; in other words, the spectrum becomes softer in the brighter phase. A bright Seyfert galaxy, NGC 4151, also exhibited such a trend (Lubiński et al. 2010). On the other hand, the trend of Cen A is opposite; the spectrum became harder in the bright phase.

Cen A was found to be a gamma-ray emitter up to the TeV band, while black hole binaries and NGC 4151 are not. Therefore, the nonthermal jet component that connects to the high energy gamma-ray band is expected to exist in the X-ray band. We included one more power-law model in addition to model D and multiplied it by the absorption with a column density of $1 \times 10^{23}\ \mathrm{cm}^{-2}$; for this additional power-law component the absorption is needed to be below the observed flux in the soft X-ray band, and the above value is just an assumption. Later we describe the dependence of the results on this absorption. In this case, we cannot constrain the parameters of both power-law components well. In addition, the intensity of the hard power-law component becomes coupled with that of the reflection component. Then, we replaced the PEXRAV model by the PEXMON model (Nandra et al. 2007) for the reflection component. The PEXMON model considered the Fe–K and Ni–K fluorescence lines and thus we can constrain the reflection component by the prominent Fe–K line. In this case, the Gaussian model for the Fe–K line is not included for fitting (model E).

Figure 10 shows a confidence contour between the soft and hard power-law photon index, where we plot the 95% confidence contours of the three 2009 observations. The photon index of the

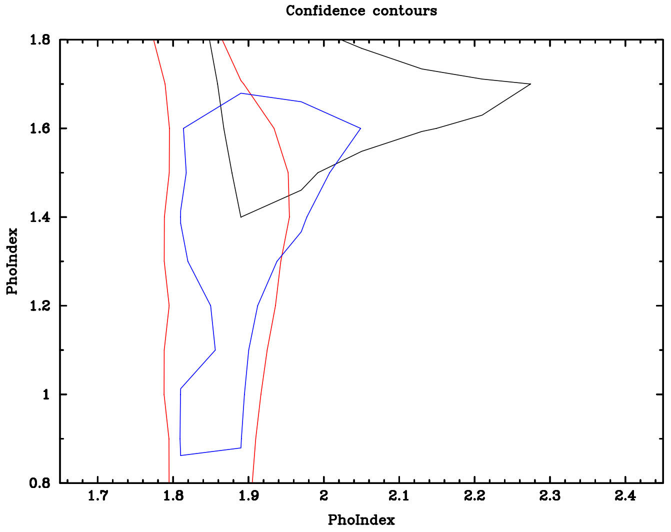

Figure 10. Confidence contour between the soft and hard power-law photon index for fitting with model E. The contours represent a 95% confidence level for each observation. Black solid, red dashed, and blue dotted lines correspond to those of the first, second, and third observations of 2009, respectively.

(A color version of this figure is available in the online journal.)

soft and hard components is constrained to be around 1.9 and 1.6, respectively, for all 2009 observations. The photon index of the hard component depends on the assumed absorption; when the absorption is weaker, the photon index becomes smaller and the fraction of the hard component in the softer X-ray band becomes smaller. Thus the photon index of 1.6 is considered to give an upper limit of the hard component. Then, we fixed the photon indices of the two power-law components to 1.6 and 1.9. Table 8 summarizes the fitting results, and Figure 11 shows the best-fit model and spectra. The χ^2 value is smaller than those of model D for the first 2009 observation, but almost the same as those of model D for others. The fraction of the reflection component is around 0.4–0.5 and the Fe abundance is around 0.7–0.9 solar. These are typical values for Seyfert galaxies, and therefore reasonable values; it can be said that we correctly modeled the reflection component. The flux of the additional power-law component was <10% and 30% of the original power law at 100 keV in 2005 and 2009, respectively.

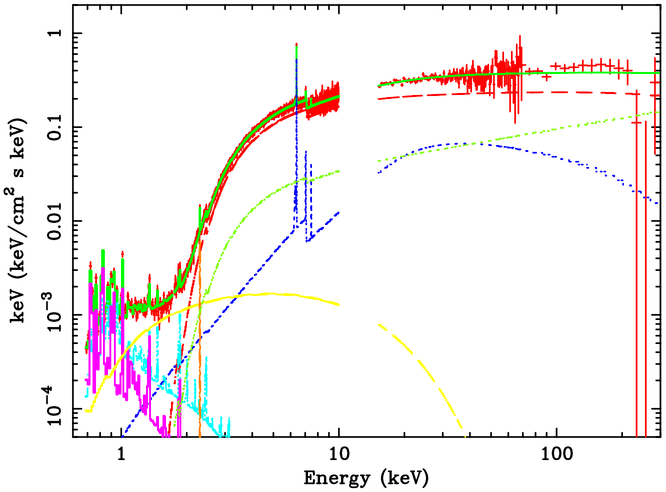

Figure 11. $\nu F \nu$ plots of the XIS/PIN/GSO spectra of the second observation of 2009 with model E.

(A color version of this figure is available in the online journal.)

Therefore, the flux increase of the additional hard power-law component, possibly associated with the jet, can explain the harder spectra in 2009, but the Seyfert-like component is still dominant in the *Suzaku* X-ray band even if the jet component exists.

3.6. Time History of Spectral Parameters

In order to check the view of model E, we performed time-resolved spectral fittings for the 2009 observations. We divided the XIS, PIN, and GSO data of each observation into 11–14 periods as a step of 10 ks. Each period corresponds to each bin of the light curve in Figure 2. Since the signal-to-noise ratio is low, we fixed the following parameters to the best-fit values obtained from the time-averaged spectra of each observation in Table 8: reflection fraction, normalization of reflected power-law emission, Fe abundance of the absorber and reflector, normalization of the S–K line, and parameters of the soft thermal components. The free parameters are the column density of the uniform absorber, the column density and covering fraction of the thicker absorber, and normalizations of

Table 8

Results of Simultaneous Fitting of the XIS/PIN/GSO Spectra (Model E)

Parameters	Unit	2005	2009a	2009b	2009c
N_H[a]	(10^{23})	1.13 ± 0.01	1.11 ± 0.01	1.12 ± 0.02	1.18 ± 0.01
A_{Fe}[b]	(Solar)	0.73 ± 0.03	1.01 ± 0.08	0.91 ± 0.07	0.72 ± 0.06
I_{pow}[c]		$0.147^{+0.001}_{-0.005}$	$0.178^{+0.009}_{-0.014}$	$0.153^{+0.006}_{-0.012}$	$0.141^{+0.009}_{-0.013}$
$N_{H,2}$[d]	(10^{24})	0.42 ± 0.07	1.84 ± 0.26	0.51 ± 0.08	1.12 ± 0.24
f_{NH2}[e]		0.20 ± 0.01	0.26 ± 0.01	0.17 ± 0.01	0.14 ± 0.01
R[f]	($\Omega/2\pi$)	0.456 ± 0.002	0.370 ± 0.002	0.409 ± 0.003	0.520 ± 0.003
I_{pow2}[g]	(10^{-3})	$0.0^{+1.3}_{0.0}$	$26.2^{+6.0}_{-2.1}$	$20.2^{+7.3}_{-3.0}$	$31.8^{+6.5}_{-4.4}$
χ^2/dof		1.41	1.37	1.11	1.23
(χ^2, dof)		(1760.5/1245)	(1900.3/1390)	(1505.7/1351)	(1681.6/1367)

Notes. Model E is `constant*phabs*([pcfabs*highecut*zvphabs*powerlaw + phabs*pexmon + phabs*powerlaw] + apec + apec + phabs*bremss + zgauss)` in XSPEC. Components between parentheses [ ] represent the AGN emission.

[a,b] Hydrogen column density and Fe abundance of the absorber. The column density is in units of cm^{-2} for the ZVPHABS model.

[c] Normalization at 1 keV of the power-law model with a fixed photon index of 1.9.

[d,e] Hydrogen column density and covering fraction of the absorber for the PCFABS model.

[f] Fraction of the reflection component for the PEXMON model.

[g] Normalization at 1 keV of the additional power-law model with a fixed photon index of 1.6.

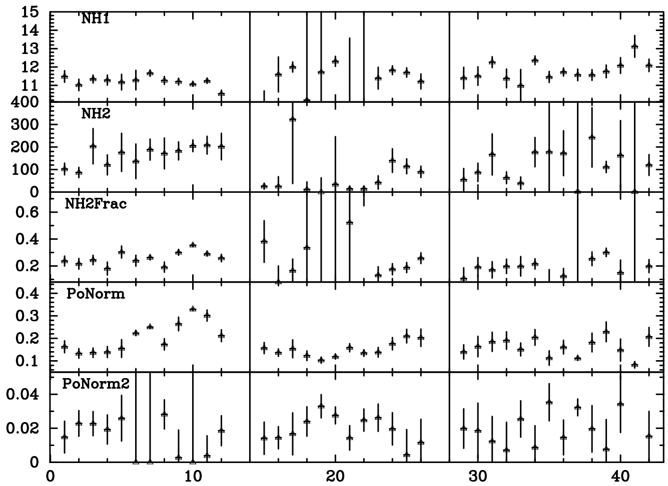

Figure 12. Time history of the spectral parameters of model E for the 10 ks time-resolved spectra in the 2009 observations. The horizontal number corresponds to the time bin number in Figure 2. From top to bottom, a uniform absorption column density in units of 10^{22} cm^{-2}, a partial covering absorption column density in units of 10^{22} cm^{-2}, a partial covering fraction of absorption, and normalizations of the soft and hard power-law components in units of photons cm^{-2} s^{-2} keV^{-1} at 1 keV are shown.

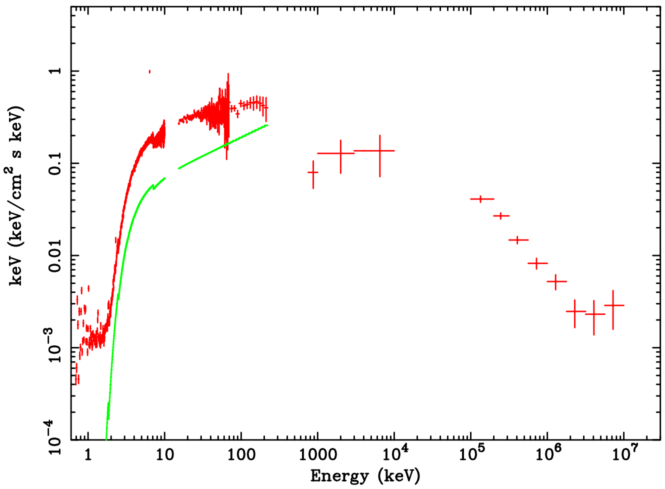

Figure 13. $\nu F \nu$ plots of the Cen A from the X-ray to GeV gamma-ray band. Data points are obtained with the *Suzaku* (2009), *CGRO*/COMPTEL (1991–1994), and *Fermi*/LAT (2008–2009). The solid line represents the hard power-law component suggested by the *Suzaku* observation.

(A color version of this figure is available in the online journal.)

two power-law components. In addition, we ignored the data below 3 keV, where the thermal component is dominant.

Figure 12 shows a time history of spectral parameters. The column density of the uniform absorber is less variable, with at most 10% variability. The most variable parameters are the normalization of the lower energy power-law component, the column density, and the covering fraction of the thicker absorber. This could create a complex correlation behavior in Section 3.1. The normalization of the higher energy power-law component is almost constant, but a small variability is seen in the third observation. It shows an anticorrelation with the normalization of the lower energy power-law component, and therefore this could be artificial. No clear correlation between the lower and higher energy power-law components suggests a different origin between two components.

4. DISCUSSION

In summary, we measured the broadband X-ray spectral variability of Cen A more accurately than ever with *Suzaku* and found that the variable component is a power law with a partially covering Compton-thick absorption of $\sim 10^{24}$ cm^{-2}. We also found a variability of the Fe–K line intensity from 2005 to 2009 by a factor of 1.3 or so. The reflection component associated with the Fe–K line is also suggested in the spectral modeling, and an additional hard power-law component with a photon index of <1.6 is inferred.

4.1. Origin of X-Ray Time Variability

X-ray time variability of the Cen A has been reported with *CGRO*/BATSE, *CGRO*/OSSE, *RXTE*, *XMM-Newton*, *INTEGRAL*, and *Swift*/BAT for various timescales from sub-days to years (Kinzer et al. 1995; Wheaton et al. 1996; Rothschild et al. 1999, 2006; Evans et al. 2004).

RXTE and *INTEGRAL* observations reported that the time variability is caused by the change of the absorption column density, the power-law photon index, and the power-law normalization, based on the spectral fitting by a power-law model with a uniform absorption (Rothschild et al. 2006). The absorption column density is in the range of $(0.9\text{–}1.7) \times 10^{23}$ cm^{-2}, the power-law photon index is in the range of 1.65–1.85, and the flux is $(4\text{–}10) \times 10^{-10}$ erg cm^{-2} in 20–100 keV. For the *Suzaku* observations (Table 3), the column density is $(0.9\text{–}1.2) \times 10^{23}$ cm^{-2}, the power-law photon index is in the range of 1.65–1.82, and the power-law flux in 20–100 keV is 5.7×10^{-10} erg cm^{-2} s^{-1} and 11×10^{-10} erg cm^{-2} s^{-1} in 2005 and 2009, respectively, based on the same model. Therefore, the spectral parameters match the past observations. However, the accurate spectroscopy with *Suzaku* revealed that a power-law model with a uniform absorption was not valid, and the X-ray variation is partly caused by the change of the partial covering Compton-thick absorber, together with the change of the power-law continuum level with a timescale of sub-days. The absorption column density of the uniform one is almost constant around 1.2×10^{23} cm^{-2}.

The variability of the Fe–K line has never been reported in past observations; it is steady around 5×10^{-4} photons cm^{-2} s^{-1}. *Suzaku* for the first time confirmed that the Fe–K line intensity significantly increased by a factor of several tens of percents from 2005 to 2009, following the brightening of the continuum flux since 2007. This suggests that the Fe–K line emitter lies at a distance of <1 pc from the nucleus. The Fe–K line intensity observed with *Suzaku* is $(2.3\text{–}3.0) \times 10^{-4}$ photons cm^{-2} s^{-1}, and therefore it is relatively weaker than ever. *RXTE* results reported that the Fe–K line intensity was around 5×10^{-4} photons cm^{-2} s^{-1} in 2004, just before the *Suzaku* 2005 observation. However, we must take care that the *RXTE* energy resolution of $\sim$1000 eV cannot accurately resolve an Fe–K line with an EW of $\sim$100 eV. *Chandra* and *XMM-Newton* results of $(2\text{–}4) \times 10^{-4}$ photons cm^{-2} s^{-1} (Evans et al. 2004) were close to the *Suzaku* ones.

The behavior in the soft gamma-ray band was well studied with the OSSE (Kinzer et al. 1995); the spectral cutoff shape varied in such a way that the cutoff was clearer in the bright phase (0.6 keV cm^{-2} s^{-1} at 100 keV) than in the faint phase (0.2 keV cm^{-2} s^{-1} at 100 keV). *Suzaku* 2005 data correspond to the faint phase and the 2009 data to the bright phase. However, the spectral cutoff is not clearly detected with *Suzaku* both in 2005 and 2009. This would be related to the additional power-law component, and we discuss this issue in the following subsection.

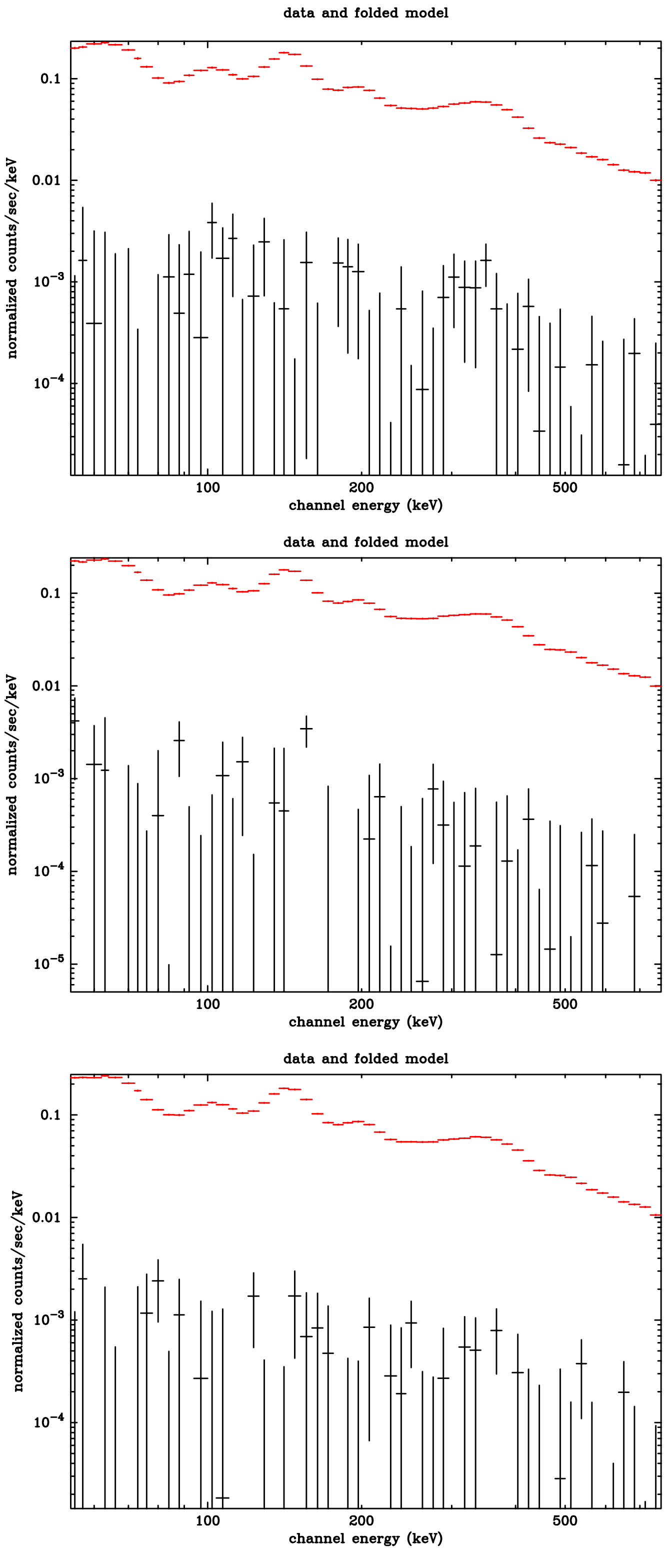

Figure 14. Comparison of GSO spectra between the data and background model during the Earth occultation period in each observation.

(A color version of this figure is available in the online journal.)

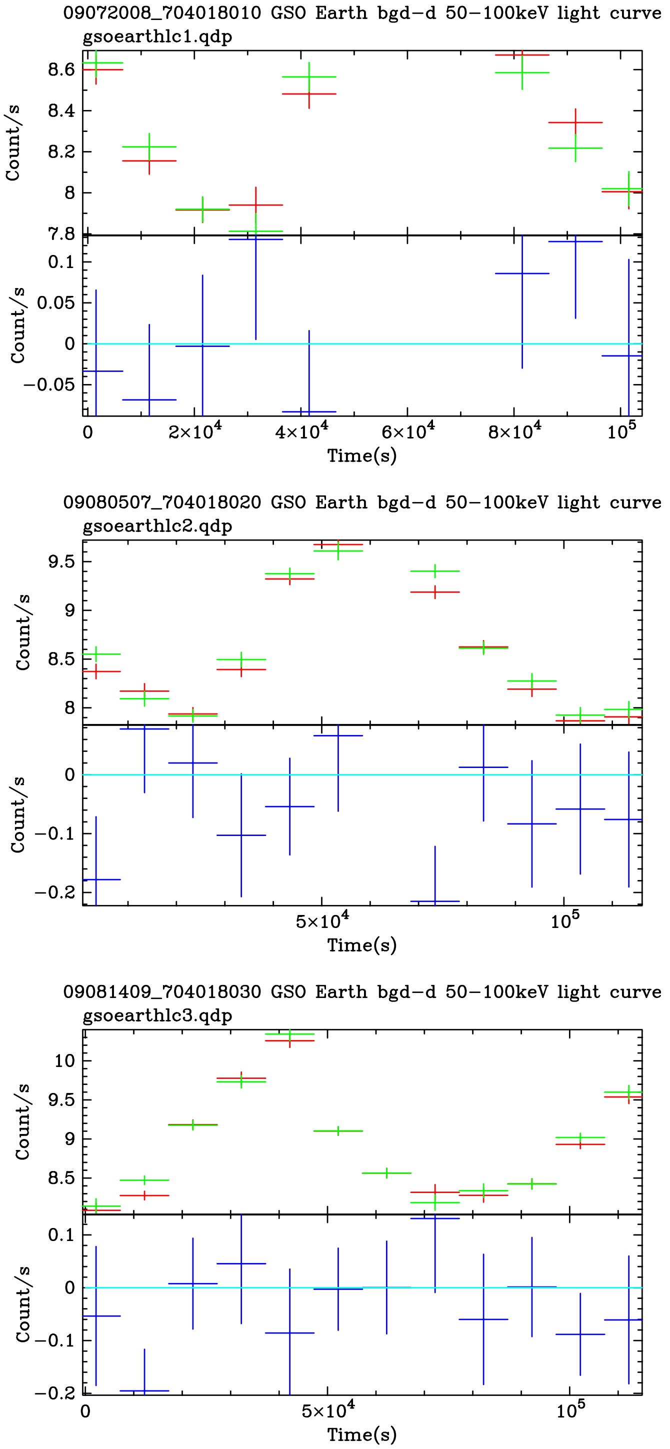

Figure 15. Comparison of GSO light curves in 50–100 keV between the data and background model during the Earth occultation period in each observation.

(A color version of this figure is available in the online journal.)

4.2. X-Ray Reprocessing Materials

The location of the stable uniform absorber can be constrained by the Fe–K edge, which is almost attributed to the uniform absorber for the time-averaged spectra. The edge energy was 7.12 ± 0.03 keV in 2009, leading to the ionization parameter of $\xi = L/nR^2 \leqslant 0.1$, where L is the luminosity of the central engine, n is the matter density, and R is the distance to the matter (Kallman et al. 2004). Considering the column density $N_{\rm H} < nR$, the uniform absorber lies at >160 pc away from the nucleus, where we take $L = 5 \times 10^{42}$ erg s^{-1} and $N_{\rm H} = 1 \times 10^{23}$ cm^{-2}. Therefore, the uniform absorber is likely to be associated with the famous dust lane lying on the elliptical galaxy.

On the other hand, the location of the thicker partial covering absorber can be constrained by the Fe–K edge in the difference spectra between high and low flux states; the edge energy is $<$7.3 keV, corresponding to $\xi \leqslant 10$. In the same way as above, using $N_{\rm H} = 10^{24}$ cm^{-2}, the location is constrained to be $R > 0.16$ pc. The variation of absorber parameters with a timescale of $\delta t \sim 1$ day indicates the blob-like structure. Taking the black hole mass of $5 \times 10^7\ M_\odot$, the Kepler velocity is $v = 1.1 \times 10^8$ cm s^{-1} at a radius of 0.16 pc. Then, the size of blobs perpendicular to the line of sight becomes $v\delta t \sim 10^{13}$ cm. Since the size toward the line of sight is likely to be the same order as above, the density becomes $n \sim 10^{11}$ cm^{-3}.

The Fe–K line EW is typical for Seyfert galaxies with a similar absorption column density (Fukazawa et al. 2011). This indicates that there is a Compton-thick material covering a large solid angle of $\sim\pi$ or so. Considering the variation timescale of $<$2 years, the material is a molecular torus, which is believed to exist commonly in Seyfert galaxies. The intrinsic emission irradiating the material is unlikely to be the beamed jet emission, since the jet emission concentrates within a small solid angle along the jet direction through the relativistic effect. Therefore, the Seyfert-like emission, originating from the inner disk region, is thought to dominate in the X-ray band.

4.3. Jet Component

Our analysis of the *Suzaku* data suggests an additional hard power-law component with a photon index of $<$1.6, whose flux is around 30% of the total flux at 100 keV. This hard component might have been brighter in the active phase of 2009 than in the faint phase of 2005. The crossover energy against another power-law emission, which is likely to be a Seyfert-like nuclear emission dominated below 100 keV, is around 400 keV. This hard component seems to smoothly connect to the *CGRO*/COMPTEL MeV gamma-ray emission as shown in Figure 13. *CGRO*/EGRET and the *Fermi* Large Area Telescope (LAT) detected the GeV gamma-ray emission from the Cen A, whose spectrum connects well to the MeV emission. As reported by Abdo et al. (2010c), the multi-wavelength spectrum of the Cen A can be modeled by the synchrotron self-Compton model. The predicted jet flux in the X-ray band strongly depends on the model parameters, such as magnetic field, emission size, low energy electron spectrum, and so on (Abdo et al. 2010c). Both the decelerating jet (Georganopoulos & Kazanas 2003) and the structure jet (Chiaberge et al. 2000) can explain the X-ray emission inferred in this paper, and the possible hard component obtained by the *Suzaku* data could be a lower energy part of the Compton component.

Evans et al. (2004) suggested the jet emission in the soft X-ray band with a photon index of around 2 and a flux of $\sim 1 \times 10^{-2}$ keV cm^{-2} s^{-1}. This flux is somewhat lower than the hard component suggested with *Suzaku*, but could be the same component. However, as Evans et al. (2004) described, their soft component can be explained by the leaked nuclear component due to the partial covering absorber. Or, since Evans et al. (2004) did not include the reflection continuum in the spectral model, their soft component could be a reflection continuum, which we considered in the spectral fitting. Alternatively, their soft component might be synchrotron emission from jets and the X-ray band covers the transition region from synchrotron emission to inverse-Compton scattering. Eitherway, we cannot conclude whether their origins are the same or not.

Jet emission has been detected in the X-ray band for radio galaxy 3C120 with *Suzaku* (Kataoka et al. 2007), where the variable soft X-ray component was detected with a shorter timescale than the Seyfert-like nuclear emission. For Cen A, the possible jet X-ray component has a longer timescale of variability than the Seyfert-like emission. Considering that GeV gamma-ray emission shows no significant variability over one year (Abdo et al. 2010c), the jet emission is less beamed and thus the relativistic effect on the variability is smaller. The jet emission in the X-ray band is often not well understood for other radio galaxies. The ASTRO-H Soft Gamma-ray Detector will give us the first opportunity to detect the hard excess component clearly from Cen A and other radio galaxies. Also, ASTRO-H can search for the jet emission from the X-ray spectral variability with the sensitive wide-band X-ray spectroscopy, as well as Cen A and 3C120.

The authors thank Dr. J. Kataoka and the anonymous referee for their careful reading and helpful comments. The authors also thank all members of the *Suzaku* Science Working Group for their contributions to the instrument preparation, spacecraft operation, software development, and in-orbit calibration. This work is partly supported by Grants-in-Aid for Scientific Research by the Ministry of Education, Culture, Sports, Science and Technology of Japan (20340044).

APPENDIX

GSO BACKGROUND REPRODUCIBILITY FOR THE Cen A DATA

Since the GSO signal rate from Cen A is less than 10% of the GSO background, the systematic uncertainty of the GSO background reproducibility is not ignored. We checked the reproducibility by using the Earth occultation data from the 2009 Cen A observation. Since the CXB is negligible, we expect no extra signal beyond the background. Figure 14 shows the comparison of GSO spectra between the Earth occultation data and the background model, indicating that the background model reproduces the Earth occultation spectra well with an accuracy of about 2%. Figure 15 shows the comparison of the GSO light curve between the Earth occultation data and the background model, indicating that the background model well reproduces the history of the Earth occultation rate with an accuracy of about 2%. Therefore, the background reproducibility is as good as 1%.

For the 2005 observation, no Earth occultation occurred during the observation. However, the background rate is lower than the 2009 observation by a factor of $\sim$2. Therefore, the effect of the background uncertainty is expected to be smaller.

REFERENCES

Abdo, A. A., Ackermann, M., Ajello, M., et al. 2009a, ApJ, 700, 597
Abdo, A. A., Ackermann, M., Ajello, M., et al. 2009b, ApJ, 699, 31
Abdo, A. A., Ackermann, M., Ajello, M., et al. 2010a, ApJ, 715, 429
Abdo, A. A., Ackermann, M., Ajello, M., et al. 2010b, ApJ, 720, 912
Abdo, A. A., Ackermann, M., Ajello, M., et al. 2010c, ApJ, 719, 1433
Abdo, A. A., Ackermann, M., Ajello, M., et al. 2010d, Science, 328, 725
Aharonian, F., Akhperjanian, A. G., Anton, G., et al. 2009, ApJ, 695, L40
Anders, E., & Grevesse, N. 1989, Geochim. Cosmochim. Acta, 53, 197
Balucińska-Church, M., & McCammon, D. 1992, ApJ, 400, 699
Beckmann, V., Jean, P., Lubiński, P., & Terrier, R. 2011, A&A, 531, A70
Chiaberge, M., Capetti, A., & Celotti, A. 1999, A&A, 340, 77
Chiaberge, M., Celotti, A., Capetti, A., & Ghisellini, G. 2000, A&A, 358, 104
Croston, J. H., Kraft, R. P., Hardcastle, M. J., et al. 2009, MNRAS, 395, 1999
Del Santo, M., Malzac, J., Jourdain, E., Belloni, T., & Ubertini, P. 2008, MNRAS, 390, 227
Dickey, J. M., & Lockman, F. J. 1990, ARA&A, 28, 215

Evans, D. A., Kraft, R. P., Worrall, D. M., et al. 2004, ApJ, 612, 786
Fukazawa, Y., Hiragi, K., Mizuno, M., et al. 2011, ApJ, 727, 19
Fukazawa, Y., Mizuno, T., Watanabe, S., et al. 2009, PASJ, 61, S17
Georganopoulos, M., & Kazanas, D. 2003, ApJ, 594, L27
Hardcastle, M. J., Evans, D. A., & Croston, J. H. 2006, MNRAS, 370, 1893
Hardcastle, M. J., & Worrall, D. M. 2000, MNRAS, 314, 359
Ishisaki, Y., Maeda, Y., Fujimoto, R., et al. 2007, PASJ, 59, 113
Kallman, T. R., Palmeri, P., Bautista, M. A., Mendoza, C., & Krolik, J. H. 2004, ApJS, 155, 675
Kataoka, J., Reeves, J. N., Iwasawa, K., et al. 2007, PASJ, 59, 279
Kinzer, R. L., Johnson, W. N., Dermer, C. D., et al. 1995, ApJ, 449, 105
Kokubun, M., Makishima, K., Takahashi, T., et al. 2007, PASJ, 59, 53
Koyama, K., Tsunemi, H., Dotani, T., et al. 2007, PASJ, 59, 23
Kraft, R. P., Forman, W., Jones, C., et al. 2000, ApJ, 531, L9
Kraft, R. P., Hardcastle, M. J., Sivakoff, G. R., et al. 2008, ApJ, 677, L97
Kraft, R. P., Kregenow, J. M., Forman, W. R., Jones, C., & Murray, S. S. 2001, ApJ, 560, 675
Krajnović, D., Sharp, R., & Thatte, N. 2007, MNRAS, 374, 385
Lubiński, P., Zdziarski, A. A., Walter, R., et al. 2010, MNRAS, 408, 1851
Maeda, Y., Someya, K., Ishidaet, M., et al. 2008, Suzaku Memo 2008-06: Recent update of the XRT response: III. Effective Area, available at http://www.astro.isas.jaxa.jp/suzaku/doc/suzakumemo/suzakumemo-2008-06.pdf
Makishima, K., Takahashi, H., Yamada, S., et al. 2008, PASJ, 60, 585
Markowitz, A., Takahashi, T., Watanabe, S., et al. 2007, ApJ, 665, 209
Matsushita, K., Makishima, K., Awaki, H., et al. 1994, ApJ, 436, L41
Miniutti, G., Fabian, A. C., Anabuki, N., et al. 2007, PASJ, 59, 315
Mitsuda, K., Bautz, M., Inoue, H., et al. 2007, PASJ, 59, 1
Müller, C., Kadler, M., Ojha, R., et al. 2011, A&A, 530, L11
Nandra, K., O'Neill, P. M., George, I. M., & Reeves, J. N. 2007, MNRAS, 382, 194
Neumayer, N., Cappellari, M., Reunanen, J., et al. 2007, ApJ, 671, 1329
Rejkuba, M. 2004, A&A, 413, 903
Rothschild, R., Band, D. L., Blanco, P. R., et al. 1999, ApJ, 510, 651
Rothschild, R., Markowitz, A., Rivers, E., et al. 2011, ApJ, 733, 23
Rothschild, R., Wilms, J., Tomsick, J., et al. 2006, ApJ, 641, 801
Shirai, H., Fukazawa, Y., Sasada, M., et al. 2008, PASJ, 60, S263
Silge, J. D., Gebhardt, K., Bergmann, M., & Richstone, D. 2005, AJ, 130, 406
Sreekumar, P., Bertsch, D. L., Hartman, R. C., Nolan, P. L., & Thompson, D. J. 1999, Astropart. Phys., 11, 221
Steinle, H., Bennett, K., Bloemen, H., et al. 1998, A&A, 330, 97
Takahashi, T., Abe, K., Endo, M., et al. 2007, PASJ, 59, 35
Tawa, N., Hayashida, K., Nagai, M., et al. 2008, PASJ, 60, S11
Tueller, J., Mushotzky, R. F., Barthelmy, S., et al. 2008, ApJ, 681, 113
Wang, B., Inoue, H., Koyama, K., et al. 1986, PASJ, 38, 685
Wheaton, W. A., Ling, J. C., Mahoney, W. A., et al. 1996, A&AS, 120, 545
Yamada, S., et al. 2011, PASJ, in press (arXiv:1107.4857)
Zdziarski, A. A., Gierliński, M., Mikołajewska, J., et al. 2004, MNRAS, 351, 791
Zdziarski, A. A., Johnson, W. N., Done, C., Smith, D., & McNaron-Brown, K. 1995, ApJ, 438, L63